



Blast from pressurized carbon dioxide released into a vented atmospheric chamber

P. M. Hansen¹ · A. V. Gaathaug¹ · D. Bjerketvedt¹ · K. Vaagsaether¹

Received: 31 October 2017 / Revised: 8 March 2018 / Accepted: 17 March 2018 / Published online: 30 March 2018
© Springer-Verlag GmbH Germany, part of Springer Nature 2018

Abstract

This study describes the blast from pressurized carbon dioxide (CO₂) released from a high-pressure reservoir into an openly vented atmospheric chamber. Small-scale experiments with pure vapor and liquid/vapor mixtures were conducted and compared with simulations. A motivation was to investigate the effects of vent size and liquid content on the peak overpressure and impulse response in the atmospheric chamber. The comparison of vapor-phase CO₂ test results with simulations showed good agreement. This numerical code described single-phase gas dynamics inside a closed chamber, but did not model any phase transitions. Hence, the simulations described a vapor-only test into an unvented chamber. Nevertheless, the simulations reproduced the incident shock wave, the shock reflections, and the jet release inside the atmospheric chamber. The rapid phase transition did not contribute to the initial shock strength in the current test geometry. The evaporation rate was too low to contribute to the measured peak overpressure that was in the range of 15–20 kPa. The simulation results produced a calculated peak overpressure of 12 kPa. The liquid tests showed a significantly higher impulse compared to tests with pure vapor. Reducing the vent opening from 0.1 to 0.01 m² resulted in a slightly higher impulse calculated at 100 ms. The influence of the vent area on the calculated impulse was significant in the vapor-phase tests, but not so clear in the liquid/vapor mixture tests.

Keywords Blast wave · Carbon dioxide · Rapid phase transition · Rapid evaporation · Vented explosion

1 Introduction

Accidental releases of carbon dioxide (CO₂) from a high-pressure reservoir into a confined space include complete tank ruptures and BLEVEs. Hazards associated with these CO₂ releases are related to both the harmful properties of the fluid (asphyxiation and frost injuries) and the energy release (blast waves, accelerated fragments, and dynamic loads on structures). The peak pressure and the impulse will be influenced by the initial state of the fluid, the degree of superheat, the amount of mass released, the vent opening area, and the structure geometry. Studies by Zhang et al. [1] and Clayton and Griffin [2] discuss the possible catastrophic consequences of previous CO₂ tank explosions.

Communicated by G. Ciccarelli.

✉ P. M. Hansen
perha@usn.no

¹ Faculty of Technology, Natural Sciences and Maritime Sciences, University College of Southeast Norway, Kjolnes ring 56, 3918 Porsgrunn, Norway

In a rapid expansion of a pressurized liquefied gas toward atmospheric pressure, the liquid could cross the saturation line without any boiling taking place. The liquid becomes superheated as it enters the metastable region, which is situated between the saturation line and the liquid spinodal line, inside the two-phase envelope. Eventually, the evaporation process will start, usually by heterogeneous nucleation on a solid surface, on particle impurities, or in microscopic gas cavities found on the surface. If heterogeneous nucleation is suppressed, the fluid could reach a highly superheated state close to the liquid spinodal. According to Reid [3,4], the possible generation of a shock wave caused by explosive evaporation could occur by homogeneous nucleation at the superheat limit. At this locus of states, the evaporation rate is very high. However, discussions in the published literature present divergent opinions as to what extent a rapid evaporation process is capable of producing a shock wave [5].

This paper presents small-scale experiments and simulations that describe the release of saturated pressurized CO₂ from a high-pressure reservoir at room temperature (292 K) into an openly vented atmospheric chamber. The primary aim

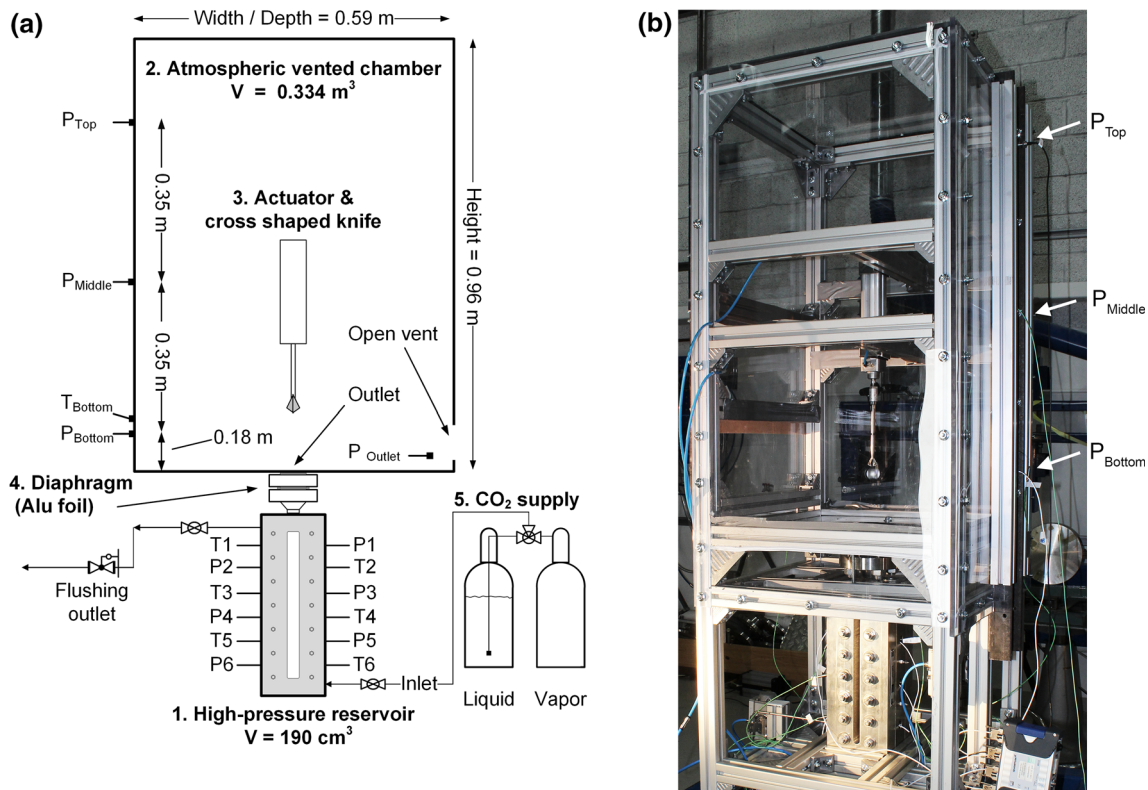


Fig. 1 **a** Schematic showing the experimental setup, **b** photograph of the high-pressure reservoir and the vented chamber

was to investigate the effects of vent opening size and initial liquid content on the measured pressure and calculated impulse response in the atmospheric chamber. An additional objective was to study whether the volume production resulting from the rapid boiling would contribute to the shock strength in the current test geometry. The results included both experimental work and a numerical simulation of the CO₂ release. The CFD model described the gas dynamics in a closed chamber and did not include any phase transitions. The experimental parameters included two different vent areas (0.1 and 0.01 m²) and three different liquid fractions (0, 32, and 68 vol%). The vent opening areas were selected based on a series of tests. Experimental work describing the depressurization and release of CO₂ from a high-pressure reservoir has previously been published [6–11], but not with a test geometry identical to the setup in the current study. Li et al. [11] describe tests in a comparable high-pressure section, but their study was mainly limited to the behavior inside the high-pressure vessel.

2 Experimental setup and methods

2.1 Apparatus

A new test setup was designed and built to study the behavior of pressurized CO₂ upon a rapid expansion toward atmo-

spheric pressure. Figure 1 shows a schematic diagram (a) and a photograph (b) of the experimental setup that consisted of the following main parts: (1) a stainless steel high-pressure reservoir, (2) an atmospheric chamber with an adjustable open vent, (3) a cross-shaped knife with a pneumatic plunger actuator, (4) an aluminum foil diaphragm, and (5) a CO₂ supply-system with two industry-grade cylinders. The two cylinders supplied liquid-phase and vapor-phase feed. Pressure sensors and temperature sensors were installed at defined positions on the experimental setup.

The high-pressure reservoir was a custom-designed level gauge rated at 10 MPa. The vessel height from the bottom up to the diaphragm was 450 mm. A bottom section, which was a rectangular duct with volume 320 × 16 × 25.4 mm³, had borosilicate glass windows that offered imaging possibilities. A circular section, which had a height of 130 mm, was located between the rectangular duct and the diaphragm. The aluminum foil diaphragm was circular with a 34-mm opening diameter. The total vessel volume was 190 cm³ with the possibility of a 130-cm³ liquid volume. Temperature sensor ports (T1–T6) and pressure sensor ports (P1–P6) were installed on the two steel sidewalls. The vertical spacing between two sensors was 50.8 mm.

The atmospheric chamber volume was 0.334 m³. The support frame, which consisted of Rexroth aluminum profiles, determined the chamber size. Transparent 10-mm polycar-

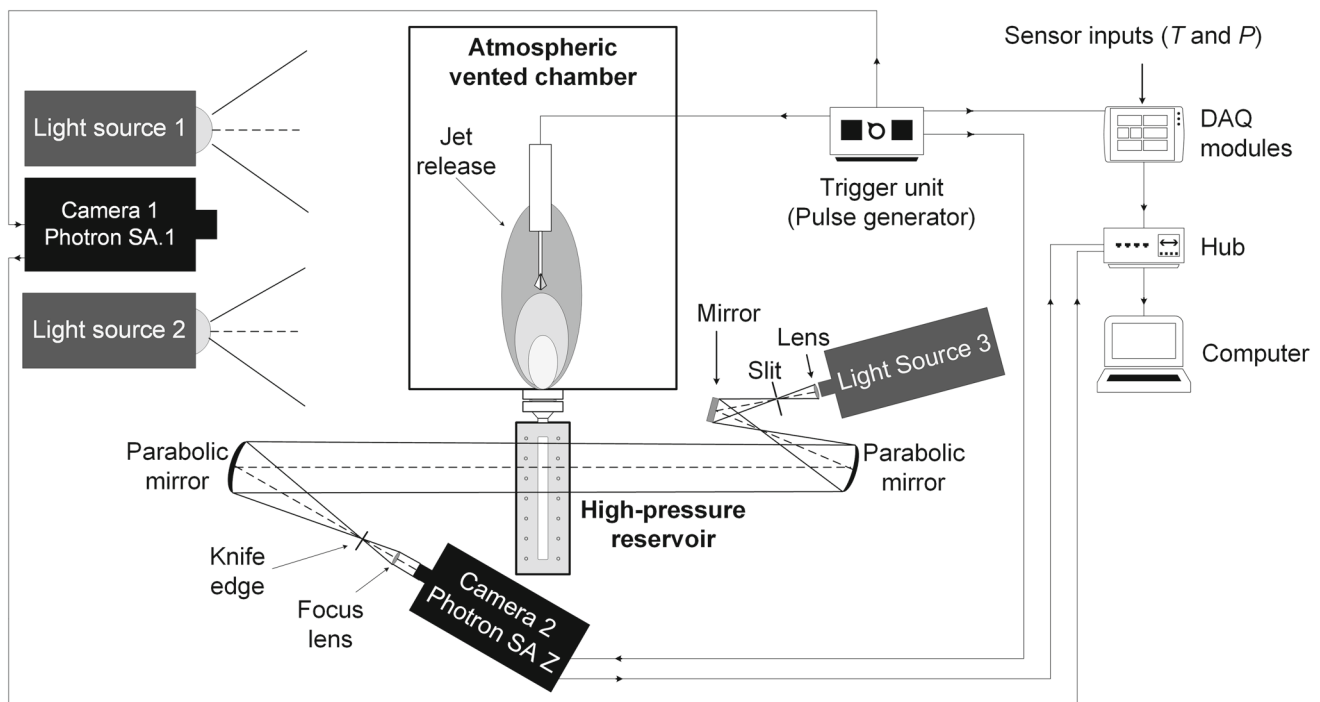


Fig. 2 Schematic of the visualization setup and the experiment control setup. Camera 1 captured the jet release into the atmospheric vented chamber while camera 2 captured the depressurization inside the high-pressure reservoir

bonate panels covered all six surfaces and enabled visual observation of the CO₂ release. The chamber dimensions were $0.59 \times 0.59 \times 0.96 \text{ m}^3$. The high-pressure reservoir and the atmospheric chamber had a volume ratio of about 1750. This resembled the release from a 1-m^3 CO₂ storage tank into a 1750-m^3 factory hall. Placing the vent at the bottom of the right sidewall, which can be seen in Fig. 1a, avoided accumulation of CO₂. The vent area A_v was fully open at all times.

2.2 Instrumentation

Four pressure sensors were installed in the atmospheric chamber. Three sensors (bottom, middle, and top) were mounted flushed to the wall on a vertical U-channel steel beam at the left sidewall. The last sensor was placed on the front sidewall perpendicular to the vent opening. One Kulite-XTM-190-100G piezoresistive transducer with a measuring overpressure range of 0–0.7 MPa and a natural frequency of 95 kHz was installed at the steel beam bottom position. The sensor accuracy was about $\pm 1\%$ of the measurement range. Pressure results from a test series gave an uncertainty estimate of $\pm 2 \text{ kPa}$.

The remaining sensors in the vented chamber were Kistler 7001 piezoelectric transducers with a measuring overpressure range of 0–25 MPa and a natural frequency of 70 kHz. The pressure transducers in the high-pressure reservoir were Kulite-XTM-190-2000G piezoresistive sensors with a mea-

suring range of 0–14 MPa and a natural frequency of 410 kHz. The accuracy was $\pm 1\%$ of the measurement range, and the thermal sensitivity shift was $\pm 2\%$ per 100 K. All temperature sensors were fast-response Chromel–Alumel, K-type thermocouples with an accuracy of $\pm 1 \text{ K}$. An Ametek Jofra CTC140A unit calibrated the temperature sensors before the start of the test series.

2.3 Camera setup and experiment control

Two high-speed cameras recorded the behavior of the CO₂ release upon diaphragm rupture in these experiments. Figure 2 shows a schematic of the visualization setup. A Photron Fastcam SA-1 operating at 5000 frames per second (fps), which used front lighting, captured the release from the high-pressure reservoir into the vented chamber. The light source was one 400-W DEB400D Dedolight and one 250-W Dedocool tungsten light head. A Photron Fastcam SA-Z operating at 75,000 fps, which was combined with a Z-type schlieren setup, captured the expansion and phase transition processes inside the high-pressure reservoir. Two parabolic mirrors combined with a focus lens covered a 0.127-m section of the vessel height.

2.4 Test procedure

Before each test, the high-pressure reservoir was flushed three times with pressurized vapor-phase CO₂ at 1 MPa. Then, the chamber was slowly filled with either vapor-phase

(TR1 and TR2) or liquid-phase CO₂ (TR3–TR5) to the desired liquid level. Visual estimations, which consisted of pixels-to-length conversion of calibrated high-speed images, provided the liquid level data. A 10 min idle period between the filling stage and the test initiation provided thermal equilibrium and stable sensor measurements. The pre-rupture state was saturated CO₂ at room temperature. A Quantum Composers 9500 series pulse generator initiated the experiments. A 5-V voltage signal simultaneously triggered the knife actuator, the high-speed cameras, and the two data acquisition systems (HBM Quantum X modules and a Sigma LDS Nicolet digital oscilloscope). The trigger signal opened the valve that filled the pneumatic knife actuator with pressurized air. The piston movement of the actuator lasted about 0.4 s, before the cross-shaped knife punctured the diaphragm completely and with high reproducibility. A shock wave then propagated outward (into the atmospheric chamber), while a rarefaction wave propagated downward (into the high-pressure reservoir). A multiphase CO₂ jet followed the initial shock wave.

The high-speed images and the sensor data were stored and then analyzed in MATLAB. High-speed videos with sensor data included were prepared. A comparison of the image observations with the sensor measurements provided a basis for the interpretation of the experimental results.

2.5 Simulation method

The 3D simulations of the CO₂ release were performed with the USN in-house CFD code [12–14]. Figure 3 shows an illustration of the simulation volume and the computational mesh. The mesh was Cartesian with one mesh length (2.5 mm) in all three directions. The simulation domain had two vertical symmetry planes to reduce computational effort. The symmetry indicated in Fig. 3 was both in the *x*–*z* and *y*–*z* planes. Hence, the simulation volume was one quarter of the full volume.

The simulation method is based on a second-order flux limiter centered (FLIC) TVD method. In addition to the mass, momentum, and energy equations, one-species transport equation is solved for CO₂ into air. The ideal gas law is used for both the gases (CO₂ and air) in the model. The governing equations are:

$$\frac{\partial \mathbf{U}}{\partial t} + \frac{\partial}{\partial x} (\mathbf{F}(\mathbf{U})) + \frac{\partial}{\partial y} (\mathbf{G}(\mathbf{U})) + \frac{\partial}{\partial z} (\mathbf{H}(\mathbf{U})) = \mathbf{0} \tag{1}$$

$$\mathbf{U} = \begin{bmatrix} \rho \\ \rho u \\ \rho v \\ \rho w \\ E \\ \rho Y \end{bmatrix}, \quad \mathbf{F}(\mathbf{U}) = \begin{bmatrix} \rho u \\ \rho u^2 + p \\ \rho uv \\ \rho uw \\ u(E + p) \\ \rho uY \end{bmatrix},$$

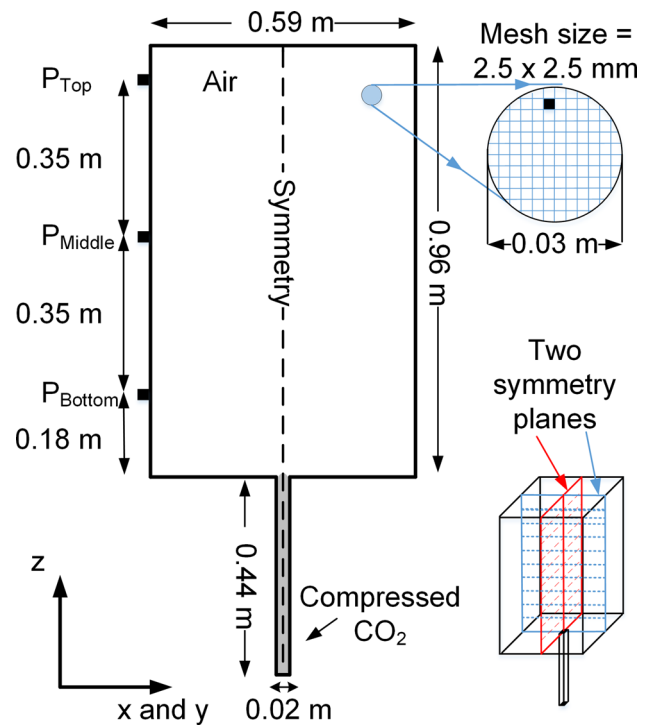


Fig. 3 Illustration of the simulation geometry and the computational mesh

$$\mathbf{G}(\mathbf{U}) = \begin{bmatrix} \rho v \\ \rho vu \\ \rho v^2 + p \\ \rho vv \\ v(E + p) \\ \rho vY \end{bmatrix}, \quad \mathbf{H}(\mathbf{U}) = \begin{bmatrix} \rho w \\ \rho wu \\ \rho wv \\ \rho w^2 + p \\ w(E + p) \\ \rho wY \end{bmatrix} \tag{2}$$

$$E = \frac{p}{\gamma - 1} + \frac{1}{2} \rho (u^2 + v^2 + w^2) \tag{3}$$

Equations (1)–(3) show the three-dimensional inviscid transport equations for mass, momentum, energy, and one species. These equations were solved by the second-order accurate, centered FLIC scheme [15] and the fractional step method [16]. The first-order fractional step method solves the transport equations in one direction at a time in sequence as one-dimensional hyperbolic equations. The Courant–Friedrich–Levy (CFL) criterion controls the time-step in the simulation for a CFL number of 0.9, meaning that the fastest wave in the domain can only propagate 90% of the mesh length in one time-step. The inviscid transport equations are chosen because the simulation results should capture the blast wave structures and the main jet-behavior. Even if the viscous stresses become large, they will not influence the wave propagation significantly in this study.

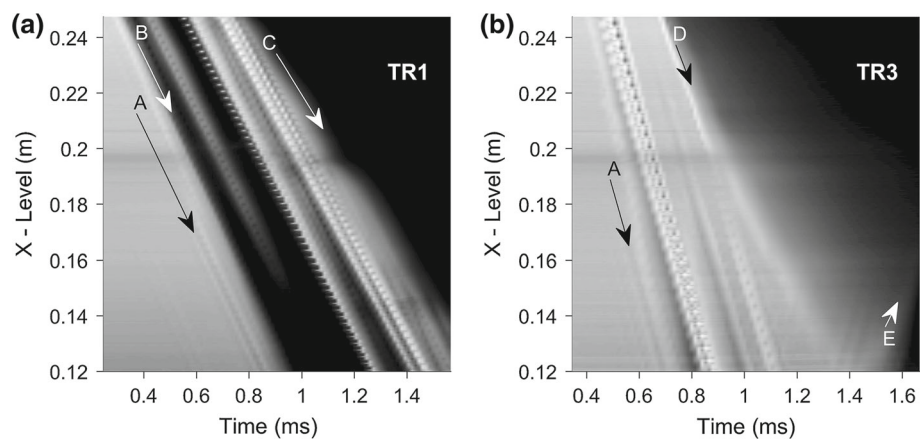
The atmospheric chamber simulation volume, which was modeled as an empty chamber, did not include any vent opening. The numerical code described single-phase gas

Table 1 Test parameters and results from the five presented test runs and the simulation

Test number	Initial pressure P_0 (MPa)	Initial temp. T_0 (K)	Open vent area A_v (m ²)	Liquid volume $V_{L,HP}$ (cm ³)	Vapor volume $V_{V,HP}$ (cm ³)	Liquid fraction (vol%)	Mass of CO ₂ m_{CO_2} (g)	Peak overpressure $P_{peak,Bottom}$ (kPa)	Impulse at 100 ms J (kPams)
TR1	5.5 ± 0.1	292 ± 1	0.1	0	190	0	36	15 ± 2	55
TR2	5.3 ± 0.1	292 ± 1	0.01	0	190	0	36	17 ± 2	149
TR3	5.6 ± 0.1	292 ± 1	0.1	130	60	68	113	20 ± 2	346
TR4	5.6 ± 0.1	292 ± 1	0.01	130	60	68	113	15 ± 2	426
TR5	5.6 ± 0.1	292 ± 1	0.01	70	120	37	77	18 ± 2	206
Simulation	5.5	292	0	0	176	0	33	12	–

Fig. 4 $x-t$ plots showing processed schlieren images recorded at 75,000 fps.

a TR1—vapor-only,
b TR3—68 vol% liquid. Arrows A–E indicate slope and position of wave phenomena. A, head of the rarefaction fan; B, C, condensation waves; D, heterogeneous nucleation at the glass surface; E, rapid boiling propagating from the duct bottom



dynamics and did not model any phase transitions. Consequently, the simulation results were only compared with vapor-only test results. Constant heat capacity ratios of $\gamma_{CO_2} = 1.28$ and $\gamma_{air} = 1.4$ were chosen. This simplification (constant gamma values) would not be valid if the primary aim was to provide accurate numerical simulations of the depressurization in the high-pressure reservoir. Because the simulations primarily focused on the blast waves and the jet release into the atmospheric chamber, this simplification could be justified. In that case, the heat capacity ratio of air would be dominant. A calculated average of C_p/R values from Masi and Petkof [17] gave the CO₂ gamma value.

3 Results and discussion

Table 1 shows test parameters and results from five presented test runs (TR1–TR5) and one simulation. The open-vent area A_v and the liquid fraction in the high-pressure reservoir were the main parameters. The initial pre-rupture state was saturated CO₂ at room temperature (292 K).

The results and discussion section was divided into the following subsections: high-pressure reservoir (Sect. 3.1), atmospheric chamber (Sect. 3.2), simulations (Sect. 3.3),

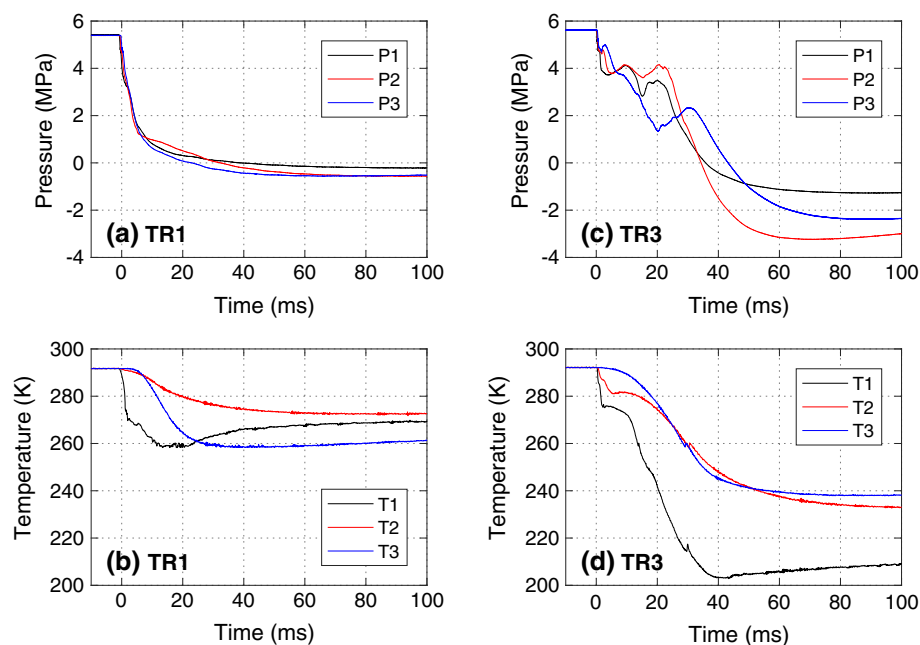
and a brief comparison of experiments and simulations (Sect. 3.4).

3.1 High-pressure reservoir

This study focused on the blast wave and the jet released into the atmospheric chamber. Nevertheless, a complete experiment description required some key results from the high-pressure reservoir. Figure 4 shows two $x-t$ plots of TR1 (a) and TR3 (b). These $x-t$ plots represent 100 processed high-speed schlieren images each that captured the initial stage of depressurization up to about 1.6 ms. Hansen et al. [7] described the preparation method that used an averaging technique to emphasize the characteristic velocities. The main disadvantage compared with stacked image series was a loss in the ability to resolve flow details. The y-axis was the visual level range in the high-pressure reservoir, starting from a position $x = 0.12$ m above the duct bottom. Upon diaphragm rupture, defined as time $t_0 = 0$ ms, a rarefaction fan propagated through the duct at the local speed of sound. Arrows (A–E) in Fig. 4a, b indicate the slope and position of the wave phenomena.

Arrows A in Fig. 4 locate the head of the rarefaction fan. The visually estimated gas-phase sound speed (200 ± 10 m/s) in Fig. 4a corresponded with the speed of sound calculated

Fig. 5 Pressure-time histories and temperature-time histories from the three upper sensor ports in the high-pressure reservoir. TR1 (vapor-only) and TR3 (liquid/vapor mixture). **a** TR1 pressure, **b** TR1 temperature, **c** TR3 pressure, **d** TR3 temperature



by the Span Wagner (SW-EOS) technical equation of state (197 m/s). Likewise, a visually estimated liquid-phase sound speed (344 ± 10 m/s) in Fig. 4b corresponded with the calculated SW-EOS value (348 m/s). Arrows *B* and *C* in Fig. 4a showed the condensation waves that followed the sudden depressurization. Arrow *D* indicated the creation of micro-size gas bubbles (heterogeneous nucleation) on the glass surface. Arrow *E* showed rapid boiling that started from the duct bottom.

The pressure traces in Fig. 5a, c showed that the duration of the expansion process depended on the initial liquid fraction. The time period increased from about 20 ms (vapor-only) to about 40 ms (68 vol% liquid). As expected, the measured temperature drop caused by the evaporation (Fig. 5d) was significantly larger than the temperature drop caused by just the vapor-expansion (Fig. 5b). At equilibrium states with pressure below the triple point ($T = 217$ K, $P = 0.518$ MPa), only solid-phase and vapor-phase CO_2 exist. Temperature measurements below 217 K in Fig. 5d suggested a solid-particle fraction greater than zero. A significant difference in temperature histories of T1 compared to T2 and T3 was observed in Fig. 5d. A possible reason could be that T1 was placed 1–2 mm into the duct, whereas T2 and T3 were placed flushed to the wall.

In Fig. 5c, the pressure decrease from the pre-rupture state at 5.6 MPa to the onset of boiling was about 0.8 MPa. Heterogeneous nucleation on the duct surfaces limited the degree of superheat that was achieved in the current test setup. According to Reid [3,4], the evaporation rate would then be too low to produce a shock wave. To achieve a higher degree of superheat in the rapid depressurization process, a smoother surface and an absence of nucleation sites would be required.

Examples of such test setups were presented by Shepherd and Simões-Moreira [18], Hill [19], Reinke [20], and Simões-Moreira [21].

3.2 Atmospheric vented chamber

All the jets observed in this study were non-stationary with an outflow duration from the high-pressure reservoir less than 100 ms. Upon diaphragm rupture, the front-lit high-speed camera did not capture the propagation of the initial blast wave into the atmospheric chamber. Moreover, the CO_2 jet was only visible when it consisted of a liquid/vapor mixture or contained solid particles. Pure CO_2 vapor would be transparent, whereas multiphase compositions appeared as an opaque white cloud.

Figure 6 shows selected high-speed video images of the CO_2 jet from TR1 (vapor-only) captured at specified times after diaphragm rupture. In Fig. 6a, a jet of partially condensed vapor was observed propagating into the atmospheric vented chamber at a vertical velocity of about 190 m/s. The knife actuator and its support frame acted as an obstacle, which is illustrated in Fig. 6b, that restricted a free jet propagation. At about 6 ms, the jet hit the top surface and was reflected downward (not visible in Fig. 6). After 10 ms, the jet diameter and height were significantly reduced. The maximum jet-diameter in the vapor-only tests was 0.11 m. Hence, the minimum distance from the pressure sensors to the edge of the jet was 0.24 m. Figure 5a shows that the high-pressure reservoir approached an atmospheric pressure after about 20 ms. These pressure measurements corresponded with the disappearance of the CO_2 cloud observed in Fig. 6c, d.

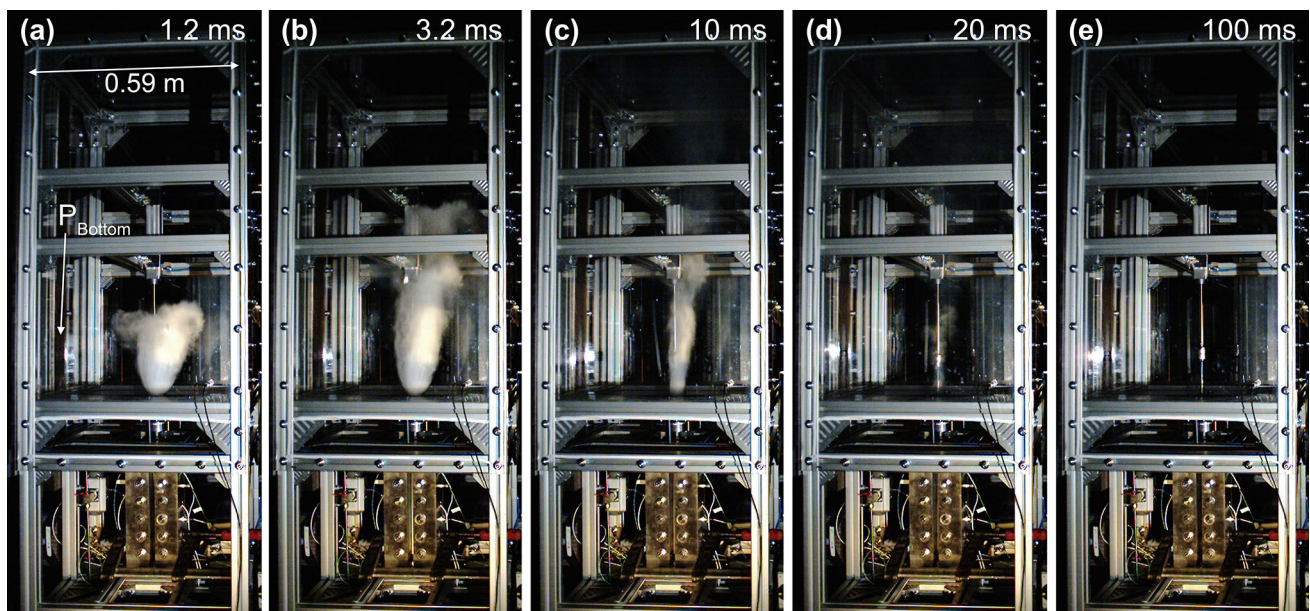


Fig. 6 Selected video frames showing the release of CO₂ vapor into the open vent chamber. TR1 (vapor-only)

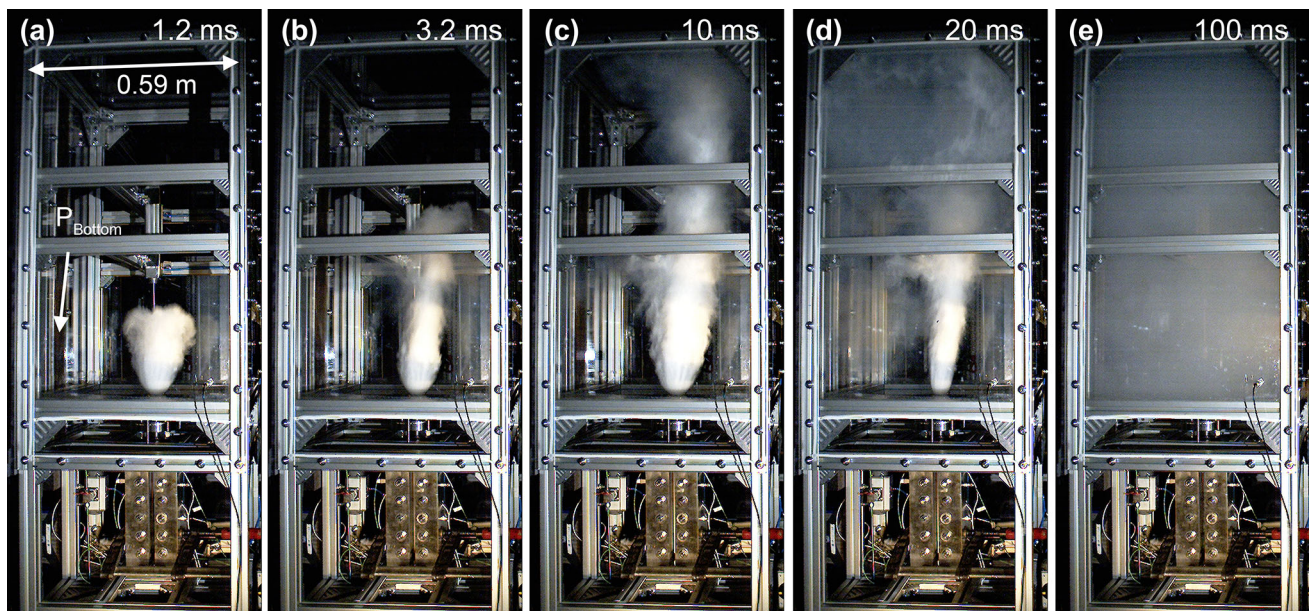


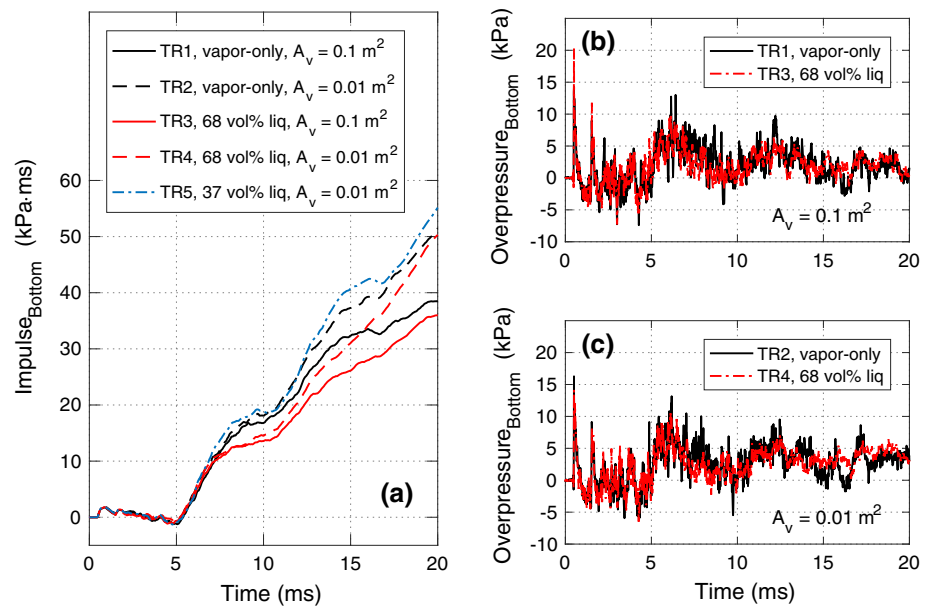
Fig. 7 Selected video frames showing the release of a liquid/vapor mixture into the open vent chamber. TR3 (68 vol% liquid)

Figure 7 shows selected high-speed video images of the jet release in TR3 (68 vol% liquid). The vertical jet velocity at the early stage was equal to TR1. In the first 3 ms after diaphragm rupture, the jet release in TR1 and TR3 appeared almost identical. No contribution from the liquid fraction in the high-pressure reservoir was observed. During this period of time, the jet behavior was governed by the expansion of the vapor headspace.

After 3.2 ms, the jet suddenly appeared more energetic, and the outflow seemed to increase (see Fig. 7c). The jet-plume diameter increased from 0.09 to 0.18 m. According

to earlier work [6,7] and tests not included in this article, this observation would correspond with the arrival of the liquid/vapor interphase (contact surface) at the reservoir exit plane. After 8–10 ms, the jet reached the top surface (see Fig. 7c) and was reflected downward. The video frames in Fig. 7c, d, and the pressure measurements in Fig. 5a, c show that a larger initial liquid fraction in the high-pressure reservoir resulted in a CO₂ jet with longer duration and a more vigorous appearance. The jet release period was increased from ≈ 20 ms (vapor-only) to ≈ 40 ms (liquid/vapor mixture). After 50–100 ms, the vented chamber was filled with

Fig. 8 **a** Impulse calculations, **b, c** pressure measurements from the vented chamber bottom sensor. 0–20 ms after diaphragm rupture. Five tests (TR1–TR5), two vent areas (0.1 and 0.01 m²), and three liquid ratios (0, 37, and 68 vol% liquid)



a white mist (Fig. 7e). The sudden temperature decrease ($\Delta T \approx 16$ K) could condense some of the water in the air that was originally present in the atmospheric chamber. Hence, a fraction of the observed mist could originate from micro-size water droplets.

The high-speed videos showed periodic wall oscillations inside the vented chamber because of multiple shock reflections (not seen in Figs. 6, 7). High-frequency vibrations originating from the initial shock wave propagated along the U-channel steel beam. These vibrations were more dominant in the middle and top sensor positions. The Kulite sensor (bottom position) seemed less sensitive to these vibrations than the Kistler sensors (top, middle, and outlet) in the present experimental study. In addition, it could provide measurements for a longer time period because of the piezoresistive operation. For these reasons, the presented pressure histories from the vented chamber originated from the Kulite bottom sensor.

The measured peak overpressure from the initial blast wave in TR1–TR5 was in the range from 15 to 20 kPa. Figure 8 shows one impulse plot and two pressure plots from the first 20-ms period. The pressure histories in the atmospheric chamber suggested the evaporation process was too slow in the current test geometry to contribute to the initial shock strength. In this study, the gas dynamics dominated the pressure response in the atmospheric chamber. No additional peaks or pressure increase could be related to the boiling liquid released from the high-pressure reservoir in the period from 0 to 20 ms. Figures 4b and 5c in Sect. 3.1 showed that the degree of superheat achieved in the high-pressure reservoir was limited by heterogeneous nucleation. These observations suggested that adiabatic evaporation at a more

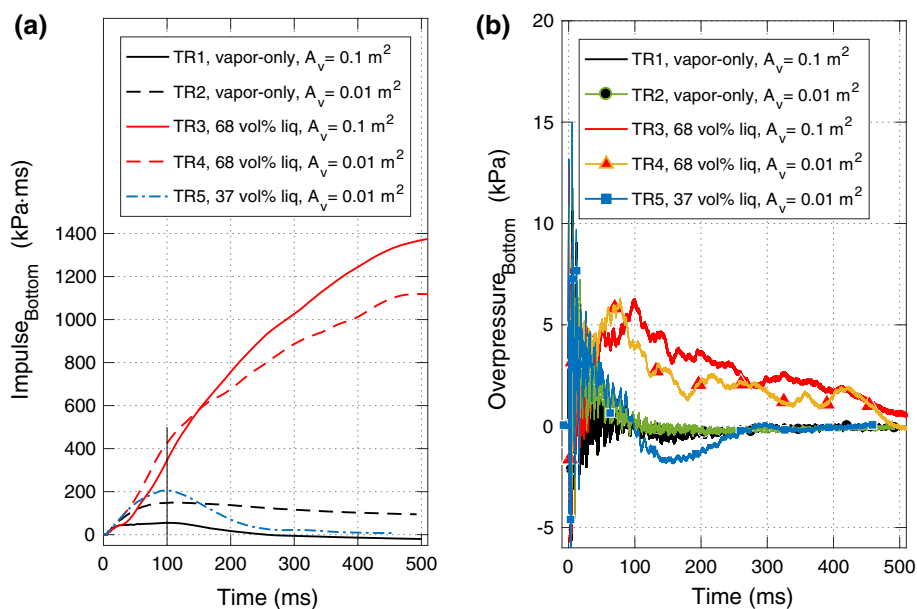
moderate degree of superheat would not contribute to the shock wave.

The calculated impulses in Fig. 8a were almost identical up to about 7 ms. Then, the impulse in the tests with lowest liquid fractions (TR1, TR2, and TR5) showed a larger increase rate than the tests with the highest liquid fractions (TR3 and TR4).

Figure 9 shows an impulse plot and a pressure plot from the 0–500-ms period. The pressure response in the atmospheric chamber seemed to coincide with the liquid content in the high-pressure reservoir. In TR3 and TR4, an increase from zero to 5–7 kPa was observed at the bottom pressure-sensor, starting at about 30 ms. A larger liquid content resulted in a longer time period at a positive overpressure. Consequently, the calculated impulses were significantly higher when the high-pressure reservoir contained a large liquid/vapor fraction, as compared to pure vapor. The duration of the liquid/vapor test was longer than 100 ms, because of the extra time needed to push the CO₂ cloud through the vent opening.

An unexpected crossover in the impulse histories of TR3 and TR4 was observed in Fig. 9 at $t = 150$ ms. One would expect that the smallest vent opening area ($A_v = 0.01$ m²) would result in the highest impulse because of a larger pressure buildup. A reason for the crossover could be the influence of the temperature drop on the pressure measurements in the chamber. As a conservative estimation, the impulses reported in Table 1 were calculated at 100 ms. A permanent offset originating from a thermal zero shift would result in a significant error contribution to the impulse calculations. Because of the rapid expansion and evaporation processes, the temperature decreased significantly both inside the high-pressure reservoir and in the vented chamber.

Fig. 9 **a** Impulse calculations, **b** pressure measurements from the vented chamber bottom sensor. 0–500 ms after diaphragm rupture. Five tests (TR1–TR5), two vent areas (0.1 and 0.01 m²), and three liquid ratios (0, 37, and 68 vol% liquid)



The following suggestions apply to future studies. It would be preferable to secure a nearly instantaneous release of liquid-phase CO₂ into the vented chamber, as recommended by Voort et al. [10]. This would improve the investigations concerning the effect of the rapid boiling on the blast wave pressure and calculated impulse. Further investigations should involve tests with a minimized vapor headspace that give a liquid content closer to 100%. Reducing the volume of the atmospheric chamber could be favorable when studying the effect of vent area on the measured pressure response. The possible generation of a shock wave would probably also require a high-pressure reservoir with a diverging/conical geometry.

3.3 Simulations of the CO₂ release (vapor-only, no vent)

The 3D simulations covering the 0–20-ms period were performed with the USN in-house CFD code. This numerical work reproduced the behavior of vapor-only CO₂ (no phase transitions) released into a closed chamber (no vent). The initial state was $P = 5.5 \text{ MPa}$ and $T = 292 \text{ K}$. Because the chamber walls produced a multiple of shock reflections, these simulations provided a useful aid to interpret the experimental pressure histories presented in Fig. 8. A time-series of numerical schlieren images that represented scaled density gradients is shown in Fig. 10. These time-series reproduced the incident shock wave, the shock reflections, and the CO₂ jet release. The time specified in the image frames, which covered the period from 0.6 to 18.9 ms, corresponded with the simulated pressure-time histories and impulse-time histories presented in Fig. 11. The incident shock wave, which

was observed at $t = 0.6 \text{ ms}$ in Fig. 10, gave the first overpressure peak in Fig. 11b–d.

The reflected shock shown at $t = 1.3 \text{ ms}$ in Fig. 10 gave the second overpressure peak in Fig. 11b–d. The upper surface and the sidewalls formed compression corners that produced the multiple of pressure peaks observed in Fig. 11b. The pressure wave then propagated in a vertical periodic pattern as shown in Figs. 10 and 11. The CO₂ jet interacted with the reflected shock wave at a time between 3.2 and 3.9 ms in Fig. 10. However, the reflected shock did not seem to influence the progression of the jet. Between the numerical images at 4.6 and 5.4 ms, the jet reached the top surface and was reflected downward. At 8.1 ms, the reflected CO₂ jet and a reflected shock (second cycle) arrived at the top pressure-sensor position almost simultaneously. It seemed that both the jet and the shock contributed to the pressure increase observed in Fig 11b.

3.4 Comparison: simulations and experimental results

The experimental impulse histories and pressure histories in Fig. 12 showed a good qualitative agreement with the simulations. The numerical results reproduced both the incident shock wave and the main shock reflections inside the atmospheric chamber. During the 0–20-ms period, the pressure response in the atmospheric chamber was governed by the rapid expansion of vapor-phase CO₂ from the pre-rupture state to atmospheric pressure. The simplified simulation geometry, which did not include a vent opening nor obstacles, contributed to some discrepancies in pressure histories observed in the 14–20-ms period. The gradual pressure decrease observed in the experimental results was not present

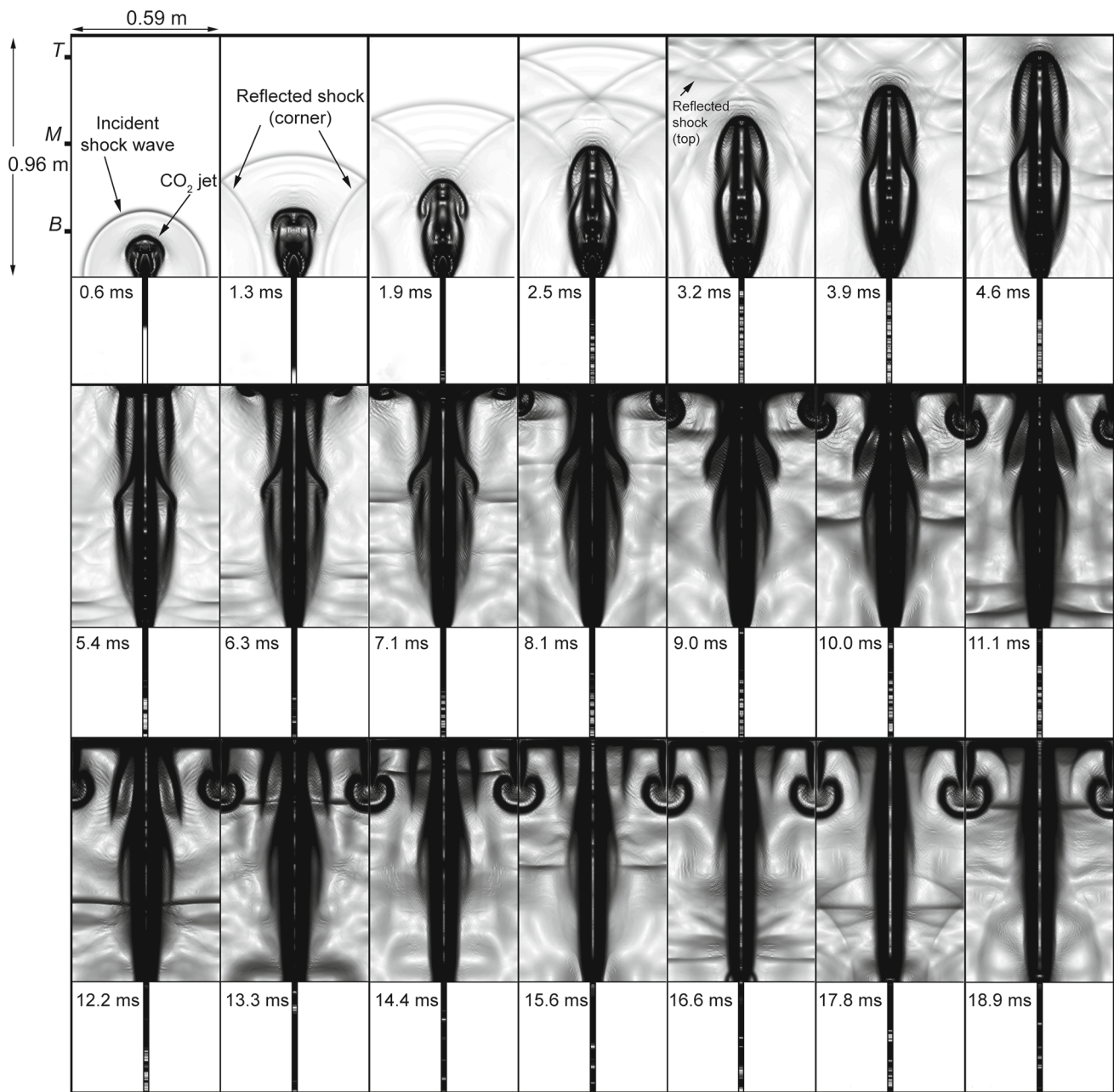


Fig. 10 Numerical schlieren time-series (0.6–18.9 ms) that represents scaled density gradients. Letters *T*, *M*, and *B* show pressure-time history positions. Simulations of CO₂ (vapor-only) released from a

high-pressure reservoir into a closed atmospheric chamber. The numerical schlieren reproduces the incident shock wave, the shock reflections, and the jet progression

in the simulations, because the simulation volume was a closed chamber.

Although the simulation code predicted the behavior of the CO₂ release in this study, it did not model phase transitions. Hence, it is not designed to model a true BLEVE. Examples of such models, which also take into account the contribution from rapid evaporation of superheated liquids, include the work by Tosse [22] and Xie [23].

4 Conclusions

This study investigated the release of pressurized CO₂ from a high-pressure reservoir into an openly vented atmospheric chamber. The pressure response was studied in a combination of small-scale experiments and simulation work. The rapid boiling did not contribute to the initial shock strength in the current test geometry. The evaporation rate was too low to contribute to the measured peak pressure that was

Fig. 11 Simulation results from the 0–20-ms period. Top, middle, and bottom sensor position. **a** Impulse histories, **b** top position pressure history, **c** middle position pressure history, **d** bottom position pressure history

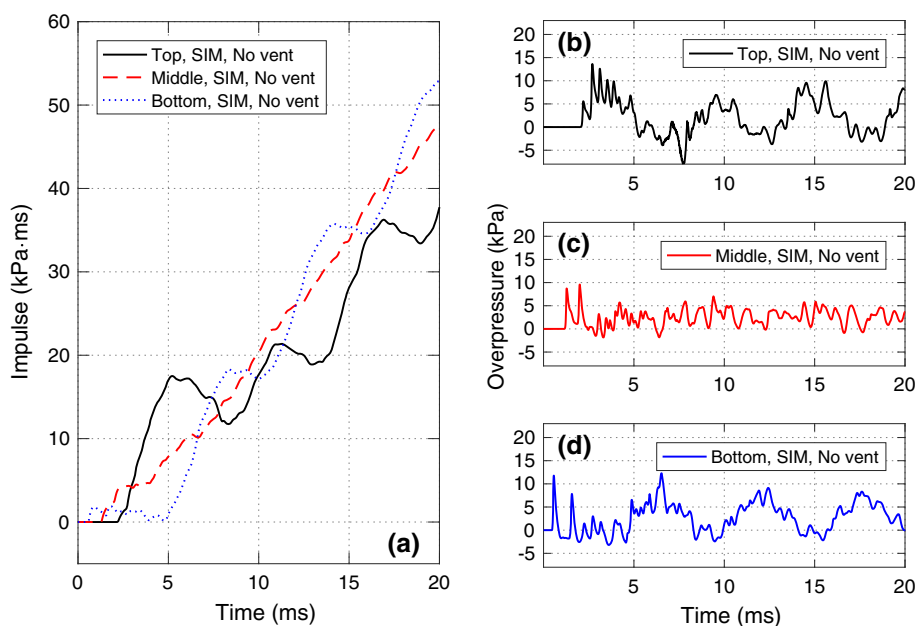
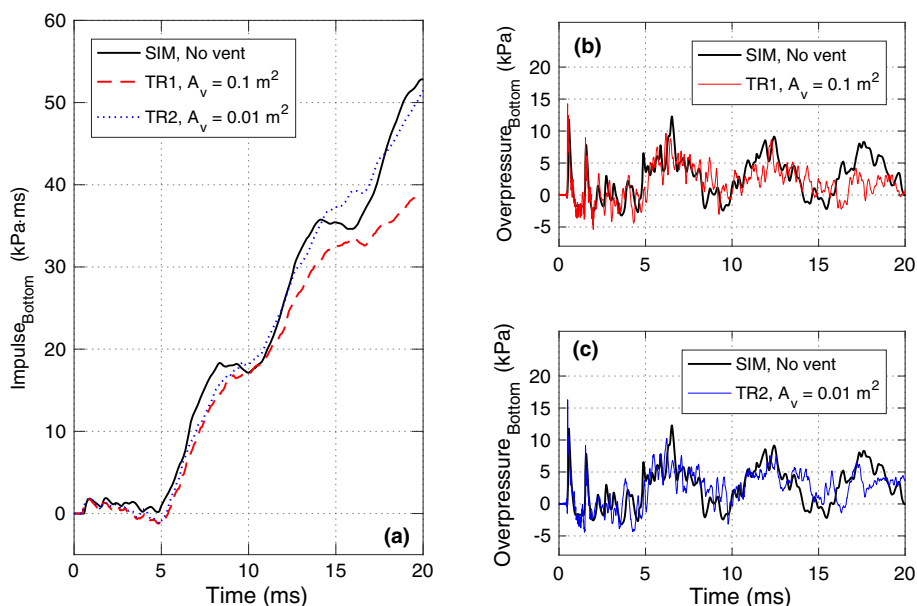


Fig. 12 Comparison of simulations and experimental results from the vented chamber bottom sensor. **a** Impulse histories, **b**, **c** pressure histories



in the 15–20 kPa range. Simulations of the vapor-only CO_2 release into a closed atmospheric chamber gave a calculated overpressure of 12 kPa. The tests with a liquid/vapor mixture in the high-pressure reservoir showed a significantly higher impulse compared to the vapor-only tests. Reducing the vent area from 0.1 to 0.01 m^2 resulted in a slight increase in impulse calculated at 100 ms. The effects of the vent area size on the impulse was evident in the vapor-only tests, but not so clear in the liquid/vapor mixture tests.

References

- Zhang, Y., Schork, J., Ludwig, K.: Revisiting the conditions for a CO_2 tank explosion. Paper presented at the AIChE 2013 Spring Meeting, San Antonio, Texas, 28 April–2 May 2013. ISBN: 9781627484480
- Clayton, W.E., Griffin, M.L.: Catastrophic failure of a liquid carbon dioxide storage vessel. *Process Saf. Prog.* **13**(4), 202–209 (1994). <https://doi.org/10.1002/prs.680130405>
- Reid, R.C.: Superheated liquids. *Am. Sci.* **64**, 146–156 (1976)
- Reid, R.C.: Possible mechanism for pressurized-liquid tank explosions or BLEVE's. *Science* **203**(4386), 1263–1265 (1979). <https://doi.org/10.1126/science.203.4386.1263>
- Birk, A.M., Davison, C., Cunningham, M.: Blast overpressures from medium scale BLEVE tests. *J. Loss Prev. Process Ind.* **20**(3), 194–206 (2007). <https://doi.org/10.1016/j.jlp.2007.03.001>

6. Tosse, S., Vaagsaether, K., Bjerketvedt, D.: An experimental investigation of rapid boiling of CO₂. *Shock Waves* **25**(3), 277–282 (2015). <https://doi.org/10.1007/s00193-014-0523-6>
7. Hansen, P.M., Gaathaug, A.V., Bjerketvedt, D., Vaagsaether, K.: The behavior of pressurized liquefied CO₂ in a vertical tube after venting through the top. *Int. J. Heat Mass Transf.* **108**, 2011–2020 (2017). <https://doi.org/10.1016/j.ijheatmasstransfer.2017.01.035>
8. Bjerketvedt, D., Egeberg, K., Ke, W., Gaathaug, A., Vaagsaether, K., Nilsen, S.H.: Boiling liquid expanding vapor explosion in CO₂ small scale experiments. *Energy Proced.* **4**, 2285–2292 (2011). <https://doi.org/10.1016/j.egypro.2011.02.118>
9. Ciccarelli, G., Melguizo-Gavilanes, J., Shepherd, J.E.: Pressure-field produced by the rapid vaporization of a CO₂ liquid column. In: *Proceedings of the 30th International Symposium on Shock Waves, Tel-Aviv* (2015). https://doi.org/10.1007/978-3-319-44866-4_87
10. Voort, M.M., Berg, A.C., Roekaerts, D.J.E.M., Xie, M., Bruijn, P.C.C.: Blast from explosive evaporation of carbon dioxide: experiment, modeling and physics. *Shock Waves* **22**, 129–140 (2012). <https://doi.org/10.1007/s00193-012-0356-0>
11. Li, M., Liu, Z., Zhou, Y., Zhao, Y., Li, X., Zhang, D.: A small-scale experimental study on the initial burst and the heterogeneous evolution process before CO₂ BLEVE. *J. Hazard. Mater.* **342**, 634–642 (2018). <https://doi.org/10.1016/j.jhazmat.2017.09.002>
12. Vaagsaether, K., Knudsen, V., Bjerketvedt, D.: Simulation of flame acceleration and DDT in H₂-air mixture with a flux limiter centered method. *Int. J. Hydrog. Energy* **32**(13), 2186–2191 (2007). <https://doi.org/10.1016/j.ijhydene.2007.04.006>
13. Gaathaug, A.V., Vaagsaether, K., Bjerketvedt, D.: Experimental and numerical investigation of DDT in hydrogen–air behind a single obstacle. *Int. J. Hydrog. Energy* **37**(22), 17606–17615 (2012). <https://doi.org/10.1016/j.ijhydene.2012.03.168>
14. Vaagsaether, K.: Modelling of gas explosions. PhD Thesis, Telemark University College/NTNU (2010). <http://hdl.handle.net/11250/2437792>
15. Toro, E.F.: *Riemann Solvers and Numerical Methods for Fluid Dynamics: A Practical Introduction*. Springer, Berlin (2009). <https://doi.org/10.1007/b79761>
16. LeVeque, R.J.: *Finite Volume Methods for Hyperbolic Problems*. Cambridge Texts in Applied Mathematics. Cambridge University Press, Cambridge (2002). <https://doi.org/10.1017/CBO9780511791253>
17. Masi, J.F., Petkof, B.: Heat capacity of gaseous carbon dioxide. *J. Res. Natl. Inst. Bur. Stand.* **48**(3), 179–187 (1952). <https://doi.org/10.6028/jres.048.025>
18. Shepherd, J.E., Simões-Moreira, J.R.: Evaporation waves in superheated dodecane. *J. Fluid Mech.* **382**, 63–86 (1999). <https://doi.org/10.1017/S0022112098003796>
19. Hill, L.G.: An experimental study of evaporation waves in a superheated liquid. PhD Thesis, California Institute of Technology (1991)
20. Reinke, P.: Surface boiling of superheated liquid. PhD Thesis, ETH Zürich (1997)
21. Simões-Moreira, J.R.: Adiabatic evaporation waves. PhD Thesis, Rensselaer Polytechnic Institute (1994)
22. Tosse, S.: The rapid depressurization and evaporation of liquefied carbon dioxide. PhD Thesis, University College of Southeast Norway (2017)
23. Xie, M.: Thermodynamic and gasdynamic aspects of a boiling liquid expanding vapour explosion. PhD Thesis, Delft University of Technology (2013)